1 **Observations of iodine monoxide over three summers at the Indian Antarctic bases, Bharati**

2 **and Maitri**

3 Anoop S. Mahajan[1*], Mriganka S. Biswas[1,2], Steffen Beirle[3], Thomas Wagner[3], Anja Schönhardt[4],

4 Nuria Benavent[5] and Alfonso Saiz-Lopez[5]

5 [1]Centre for Climate Change Research, Indian Institute of Tropical Meteorology, Ministry of Earth

6 Sciences, Pune, 411008 India.

7 [2]Savitribai Phule Pune University, Pune, 411008 India.

8 [3]Max-Planck-Institut für Chemie (MPI-C), Satellitenfernerkundung, 55128 Mainz, Germany

9 [4]Institute of Environmental Physics, Department of Physics and Electrical Engineering, University

10 of Bremen, Bremen, 330440 Germany.

11 [5]Department of Atmospheric Chemistry and Climate, Institute of Physical Chemistry Rocasolano,

12 CSIC, Madrid 28006, Spain

13

14 * corresponding author: Anoop S. Mahajan (anoop@tropmet.res.in)

15

16   **Abstract**

17   Iodine plays a vital role in oxidation chemistry over Antarctica, with past observations showing

18   highly elevated levels of iodine oxide (IO) leading to severe depletion of boundary layer ozone in

19   West Antarctica. Here, we present multi axis differential absorption spectroscopy (MAX-DOAS)

20   based observations of IO over three summers (2015-2017) at the Indian Antarctic bases, Bharati

21   and Maitri. IO was observed during all the campaigns, with mixing ratios below 2 pptv for the

22   three summers, which are lower than the peak levels observed in West Antarctica. This suggests

23   that sources in West Antarctica are different or stronger than sources of iodine compounds in East

24   Antarctica, the nature of which are still uncertain. Vertical profiles estimated using a profile

25   retrieval algorithm showed decreasing gradients, with a peak in the lower boundary layer. The

26   ground-based instrument retrieved vertical column densities (VCDs) were approximately a factor

27   of three-five higher than the VCDs reported using satellite-based instruments, which is most likely

28   related to the sensitivities of the measurement techniques. Airmass back-trajectory analysis failed

29   to highlight a source region, with most of the airmasses coming from coastal or continental regions.

30   This study highlights the variation in iodine chemistry in different regions in Antarctica and the

31   importance of a long-term dataset to validate models estimating the impacts of iodine chemistry.

32

33   Keywords: Iodine; Antarctica; halogens; DOAS

1. Introduction

Reactive halogen species (RHS) have been shown to play a critical role in causing ozone depletion events in the polar boundary layer (BL) (Barrie et al., 1988; Bottenheim et al., 1986; Kreher et al., 1997; Oltmans and Komhyr, 1986) and could contribute to new particle formation in this remote environment (Allan et al., 2015; Atkinson et al., 2012; O'Dowd et al., 2004). Observations of RHS have been made in the Antarctic BL for almost two decades. Early observations focused on bromine oxide (BrO), the presence of which was observed in the Antarctic using ground based instruments (Kreher et al., 1997) and via satellites (Hollwedel et al., 2004). The presence of iodine oxide (IO) in the Antarctic atmosphere was also confirmed through integrated column measurements from the ground (Frieß et al., 2001). Later, year-long ground-based observations of RHS made at Halley Bay showed the critical role that bromine and iodine compounds play in regulating the oxidizing capacity, causing ozone depletion and new particle formation in the Antarctic BL (Saiz-Lopez et al., 2007a). These ground-based observations showed that both IO and BrO, are present at elevated concentrations (from 1 pptv to as high as 20 pptv) in certain parts of the Antarctic BL, and show a significant seasonal variation peaking in the spring, with elevated concentrations observed through the summer (Saiz-Lopez et al., 2008). Satellite-based observations of both IO and BrO reported a similar annual cycle, although with large geographical differences (Hollwedel et al., 2004; Richter et al., 2002; Saiz-Lopez et al., 2007b; Schönhardt et al., 2008, 2012; Theys et al., 2011; Wagner et al., 2001). These satellite observations have been validated by ground-based observations, although most of them have hitherto focused around the Weddell Sea (Atkinson et al., 2012; Buys et al., 2013; Frieß et al., 2001, 2010; Saiz-Lopez et al., 2007a, 2008). Previous studies show that similar levels of BrO have been observed between the Arctic and Antarctic while much lower levels of atmospheric iodine have been reported in the

3

57 Arctic compared to the Antarctic (Hönninger et al., 2004; Raso et al., 2017; Schönhardt et al.,

58 2008; Tuckermann et al., 1997). The satellite observations also show a difference in the

59 geographical distribution of IO over Antarctica, with the Weddell sea being an iodine hotspot, the

60 reasons for which are still not completely clear (Saiz-Lopez and Blaszczak-boxe, 2016). Ground-

61 based observations have also been made at McMurdo Sound, near the Ross Sea, where lower

62 concentrations of IO were observed (Hay, 2010). Additional observations over the 2011-2012

63 summer were made at Dumont d'Urville using a cavity enhanced absorption spectroscopy based

64 instrument and showed a maximum of 0.15 pptv of IO (Grilli et al., 2013). However, observations

65 of IO have not been reported in the Indian Ocean sector of the Antarctic peninsula to date (Saiz-

66 Lopez et al., 2012; Saiz-Lopez and von Glasow, 2012).

67 Ground based observations at Halley Bay and in the Weddell Sea suggest that the main source of

68 iodine compounds is the sea ice region based on observations of iodocarbons and back trajectory

69 analysis (Atkinson et al., 2012; Saiz-Lopez et al., 2007a). Other studies have also measured

70 iodocarbons in Antarctica, although their levels are too low to explain the high levels of IO

71 observed in the Weddell Sea region (Carpenter et al., 2007; Fogelqvist and Tanhua, 1995;

72 Reifenhäuser and Heumann, 1992). The exact process is still not known, although a mechanism

73 for biologically-induced iodine emissions from sea-ice has been suggested based on the idea that

74 micro-algae (Garrison and Buck, 1989) are the primary source of iodine emissions in this

75 environment (Saiz-Lopez et al., 2015a) with halogen compounds then moving up brine channels

76 in the sea ice to finally get released into the atmosphere. There are further questions regarding the

77 propagation of reactive iodine chemistry across the continent because satellite observations show

78 the presence of IO deep within the Antarctic continent, even as far as the South Pole (Saiz-Lopez

79 et al., 2007b; Schönhardt et al., 2008). However, although enhanced, the observed IO column

4

80   densities are close to the detection limit of the satellite instrument (~7 x 10^{12} molecules cm^{-2} for a

81   single measurement) and are therefore subject to uncertainties. The study by Frieß et al. (2010)

82   suggested a strong source within the snowpack, which hints at active recycling and re-emission of

83   IO aiding the long transport inland. However, questions remain about why such a source would

84   function only in parts of the continent and why the primary source is different from the Arctic,

85   where much lower peak concentrations are sporadically observed (Mahajan et al., 2010; Saiz-

86   Lopez and Blaszczak-boxe, 2016). To further understand the sources of iodine in the polar

87   environment, understanding the geographical distribution is critical. Satellite observations play a

88   useful role for this, although validation of the satellite observations using ground-based

89   instruments is necessary to ascertain their accuracy to observe IO in the Antarctic troposphere.

90   Questions also remain about the vertical profiles of iodine compounds within and above the

91   Antarctic boundary layer. Modelling based studies using the one-dimensional Tropospheric

92   Halogen Chemistry MOdel (THAMO) have suggested a strong gradient in IO from the surface to

93   the edge of the boundary layer (Saiz-Lopez et al., 2008). Only once in the past have vertical profiles

94   of IO been measured in Antarctica using the MAX-DOAS instrument. These measurements were

95   made at McMurdo Sound in East Antarctica (Hay, 2010). Observations over two "golden days" in

96   2006 and 2007 show surface concentrations of about 1 pptv, decreasing to ~0.2 pptv at about 200

97   m, before reaching a second maximum of 0.6 pptv at ~700 m. The detection limit was estimated

98   to be about ~0.5 pptv. However, models did not reproduce this measured IO vertical profile shape

99   and there are also large uncertainties associated with the a priori (Hay, 2010). In most models, the

100   assumption is that the source of iodine compounds is from the snowpack, with photochemistry in

101   the atmosphere resulting in a steady decrease with altitude. However, considerable challenges

102   remain in reproducing the surface variation and vertical gradients in addition to the geographical

103 distribution (Fernandez et al., 2019). More recent modelling studies combined with aircraft

104 observations suggest that the gradient is not very sharp all the latitudes, with a significant free

105 tropospheric and stratospheric contribution to the total column of IO (Koenig et al., 2020; Saiz-

106 Lopez et al., 2015b), although such observations have still not been done in the Antarctic. One of

107 the main reasons for the uncertainties in models is the lack of consistent measurements of vertical

108 gradients across the world, especially in the Polar Regions, to validate these model simulations.

109 Considering the uncertainties in the satellite observations and questions regarding the sources and

110 vertical and geographical distribution of IO, further observations are necessary. Here we present

111 observations made at two new locations in Antarctica over three summers and compare them with

112 the satellite-based retrievals and past observations.

113

114 **2. Methodology**

115 Figure 1 shows the location of the two Indian Antarctic stations, Maitri (11.73 °E , 70.77 °S) and

116 Bharati (76.19 °E, 69.41 °S). The other stations where observations of IO have been reported in

117 the past are also marked on the map. Observations of IO and the oxygen dimer (O_4) were made

118 using the Multi-Axis Differential Optical Absorption Spectroscopy technique (MAX-DOAS) over

119 three summers: February-March 2015 as a part of the 34th Indian Scientific Expedition to

120 Antarctica (ISEA-34), November 2015 – February 2016 as a part of ISEA-35 and January-

121 February 2017 as a part of ISEA-36.

122 Observations at the Maitri station were made over a short span of 9 days (9th March – 17th March

123 2015) and only during ISEA-34. The research station is in the ice-free rocky area on the

124 Schirmacher Oasis. The MAX-DOAS instrument was installed in a summer-time residential

125   container, ~150 m north the station, about 120 m above sea level during the ISEA-34. The scanner

126   unit was mounted on top of the container with the clear line of sight to the horizon. The scanner

127   pointed ~60.0° with respect to magnetic north. The spectrometer unit was kept inside the container,

128   which was temperature controlled. The open ocean is 125 km north of Maitri.

129   Observations at the Bharati station were made for 10 days (9th February-18th February 2015) during

130   ISEA-34, for 63 days (30th November 2015 – 1st February 2016) during ISEA-35 and for 35 days

131   (5th January-11th February 2017) during ISEA-36. The station is located between the Thala Fjord

132   and Quilty Bay, east of the Stornes Peninsula. The MAX-DOAS instrument was installed in a hut

133   on top of a ridge around 200 m south-west of the Bharati station and was approximately 56 m

134   above sea level. The scanner unit was mounted on the wall of the hut and had a clear line of sight

135   to the horizon, pointing -23.2° with respect to the north, overlooking the open ocean. The coastline

136   is within 500 m of the hut, but it becomes ice free from mid-January to late March. Depending on

137   the sea ice conditions, the open ocean is within 8-10 km north from the end of November.

138   The MAX-DOAS instrument (EnviMes) makes use of scattered sunlight along different elevation

139   angles and by combination of several lines of sight including the zenith. The concentration of an

140   absorber in the boundary layer can be obtained either in a first approximation by a simple

141   geometric approach or by simulating the light path with a radiative transfer model taking into

142   account also multiple scattering effects and the correct treatment of the aerosol loading in the

143   atmosphere (Hönninger et al., 2004; Platt and Stutz, 2008; Wagner et al., 2004). The instrument

144   consists of an indoor unit, housing a spectrometer with a spectral resolution of 0.7 nm (UV: 301.20-

145   463.69), which is connected to an outdoor unit, containing a scanning telescope. Discrete elevation

146   angles (1°, 2°, 3°, 5°, 7°, 10°, 20°, 40°, and 90°) were recorded for a total exposure time of 1

147   minute each during all the four campaigns. The spectra were recalibrated before analysis using

148 mercury emission lines recorded at the end of each day. For DOAS retrieval, the QDOAS 3.2

149 software was used (Fayt and Van Roozendael, 2013). For estimation of the O_4 Differential Slant

150 Column Densities (DSCDs), the cross-sections of O_4 (Thalman and Volkamer, 2013) at 293K;

151 NO_2 (Vandaele et al., 1998a) at 220 K and 298 K (220 K orthogonalized to 294 K); O_3 (Bogumil

152 et al., 2003) at 223 K and 243 K (orthogonalized to O_3 at 243 K); HCHO (Meller and Moortgat,

153 2000) at 298 K; HONO (Stutz et al., 2000) at 296 K were used in the 351-390 nm window. The

154 cross-sections used for IO retrieval in the 417-440 nm spectral window were: IO (Gómez Martín

155 et al., 2005), NO_2 220 K and 298 K (Vandaele et al., 1998b), H_2O (Rothman et al., 2013), O_4

156 (Thalman and Volkamer, 2013) and O_3 (Bogumil et al., 2003). In addition to these cross-sections

157 a ring spectrum (Chance and Spurr, 1997), a second ring spectrum following Wagner et al. (2009),

158 and the 3rd order polynomial were used for both windows. The zenith spectrum from each scan

159 was used as a reference to remove contribution from possible free tropospheric or stratospheric

160 absorption. An example of a DOAS fit for O_4 and IO are given in Figure S1. Surface mixing ratios

161 and the total vertical column densities (VCDs) were retrieved from the MAX-DOAS DSCDs of

162 IO and O_4 by employing the Mainz Profile Algorithm (MAPA) (Beirle et al., 2018). Only

163 observations with solar zenith angles (SZA) less than 75° were used for the profile retrievals due

164 to the large path lengths through the stratosphere for large SZA angles. This algorithm uses a two-

165 step approach to determine the trace gas vertical profiles. In the first step, the aerosol profiles are

166 retrieved using the measured O_4 DSCDs. A Monte Carlo approach is utilized to identify the best

167 ensemble of the forward model parameters (column parameters (c) (VCD for trace gases and

168 aerosol optical depth for aerosol), height parameter (h) and shape parameter (s)), which fit the

169 measured O_4 DSCDs for the sequence of elevation angles. In the second step, the aerosol profiles

170 retrieved from the O_4 inversion are used as an input to retrieve similar model parameters (c, h, and

8

171   s) for IO. The state of the atmosphere was calculated using the pressure and temperature profiles

172   observed by the in-situ radiosondes, which were launched once a week at both stations. An

173   angstrom exponent of 1 was used for the difference in the retrieval wavelengths as per observations

174   made at Bharati in the past (Prakash Chaubey et al., 2011). Within MAPA, the differential air mass

175   factors (AMFs) are calculated offline with the radiative transfer model McArtim (Deutschmann et

176   al., 2011) for fixed nodes for each parameter and stored as a lookup table (LUT) for quick analysis.

177   To assess the quality of the retrievals, MAPA provides "valid", "warning" or "error" flags for each

178   measurement sequence, which are calculated based on pre-defined thresholds for various fit

179   parameters. For further details about MAPA, please refer to the description paper by Beirle et al.

180   (2018). Additionally, MAPA provides the option to use a scaling factor for significant mismatch

181   between the modelled and measured O_4 DSCDs, which has been shown to be close to 0.8 in the

182   past (Wagner et al., 2019). Using the variable option, where the model estimated scaling factor

183   ranged between 0.75 and 0.9. Therefore, a scaling factor of 0.8 was applied for all the campaigns.

184   We also make use of the IO vertical column densities retrieved using the SCanning Imaging

185   Absorption spectroMeter for Atmospheric CHartographY (SCIAMACHY), a UV-vis-NIR

186   spectrometer onboard the ENVISAT satellite (Burrows et al., 1995). Observations from

187   SCIAMACHY stopped due to instrumental problems in April 2012. Here we make use of the mean

188   from 2004-2011 to look at the geographical distribution and compare it with the ground-based

189   observations made during the study period. Further details about the IO retrieval algorithm and the

190   SCIAMACHY instrumental setup can be found elsewhere (Schönhardt et al., 2008, 2012).

191

192   **3. Results and Discussion**

3.1 Meteorological parameters

Figure 2 shows the 5-day back-trajectories arriving every hour at the two stations at a height of 10 m on the days that the DOAS measurements were conducted as a part of the three ISEA expeditions. The back-trajectories were calculated using the HYbrid Single-Particle Lagrangian Integrated Trajectory (HYSPLIT) using the EDAS-40 km database (Draxler and Rolph, 2003). The trajectories show that the airmasses sampled throughout the three expeditions were from either a remote oceanic region, coastal Antarctica, or the continental shelf. In general, most of the trajectories show that the airmasses had travelled over hundreds of kilometres over the last five days. For the local meteorological conditions, Figure 3 (top panels) show the wind direction at the Bharati station. Most of the time, the wind was from the ocean, with the winds coming from the north-west sector and a few instances of northern and north eastern winds (although during ISEA-34 the winds were mostly from east to north-east). This was during all the three expeditions at the Bharati station. The wind speed was mostly below 20 knots (~10 m s^{-1}) for all the campaigns, although periods of high winds were observed during ISEA-35 and ISEA-36, which were of a longer duration than ISEA-34. The temperature at the station hovered between -5 °C and +5 °C, through the summer period, with higher values closer to noon (Figure 3, middle panels). The humidity fluctuated from 40% to above 90%. The radiation followed a clear diurnal pattern, with the highest values seen around local noon and minima at local midnight. Considering that this region experiences continuous light for 24 hours, the radiation also showed a non-zero minima between November to January (Figure 3, bottom panels). However, in February, a clear night-time is seen in the radiation data. Finally, a measure of the cloudiness was also tracked using visual full sky cloud cover observations. Any cloud cover of more than 30% was considered to be cloudy (cloud flag value of 1), which helps in filtering the MAX-DOAS observations. In addition to the

10

216   visual inspection of the sky, which was performed once an hour, a second cloud index was

217   calculated based on the ratios of the radiances at 320 nm and 440 nm from the 3° and zenith spectra

218   (Mahajan et al., 2012; Wagner et al., 2014). Both manual and radiance-based indices showed a

219   close match, indicating that cloudy conditions were well discerned by the cloud index calculation.

220   Meteorological data was unfortunately not available at the Maitri station.

221   **3.2 Differential Slant Column Densities (DSCDs)**

222   Figure 4 shows the observed O_4 DSCDs at different elevation angles for all the campaigns. O_4

223   DSCDs were found to be higher at lower elevation angles, as expected, which is because the O_4

224   concentration is proportional to the square of the oxygen pressure and thus increases towards the

225   surface. This also suggests that the aerosol loading was low in the atmosphere. Photons travel

226   longer paths at lower elevation angles and interact more with tropospheric absorbing species before

227   reaching the instrument resulting in a decreasing profile with increasing elevation angles. The

228   average residual root mean square (RMS) and 2σ detection limit for the O_4 DSCDs were 4.46×10^{-4}

229   (range: $1.56\text{-}10.01\times10^{-4}$) and 2.11×10^{42} molecules^2 cm^{-5} (range: $0.72\text{-}4.66 \times 10^{42}$ molecules^2

230   cm$^{-5)}$, respectively (Figure 4). The O_4 DSCDs were then used to estimate the aerosol profiles and

231   hence the IO mixing ratios, as described earlier in section 2.

232   Figure 5 shows the observed IO DSCDs at different elevation angles for all the campaigns. The

233   IO DSCDs were found to be higher at lower elevation angles, which indicates a decreasing gradient

234   in the IO vertical profile. The residual RMS was in the $1.15\text{-}9.73\times10^{-4}$ range (mean: 3.46×10^{-4}),

235   resulting in 2σ IO DSCD detection limits of 6.57×10^{12} to 5.71×10^{13} molecules cm^{-2} (mean

236   1.88×10^{13} molecules cm^{-2}) (Figure 5). For several days, only the lowermost elevation angles were

237   found to be above the two-sigma detection limit of the instrument. Higher IO DSCDs were

11

observed at large SZAs, which is related to an increase in the path length. However, only observations with SZA<75° were used to estimate the vertical profiles and surface mixing ratios using the aerosol profiles derived using the O_4 DSCDs, as described earlier in section 2. A zoomed in view of two example days for both the O_4 and IO DSCDs is shown in Figure S2, which clearly shows the decreasing gradient with increasing elevation angles.

3.3 IO Vertical Column Densities (VCDs) and mixing ratio profiles

The O_4 and IO DSCDs were used to retrieve the vertical column densities and the vertical profiles for aerosols and IO. A comparison of the MAX-DOAS observed O_4 DSCDs with the MAPA modelled DSCDs for all the four campaigns are shown in Figure S3, and Figure S4 shows a similar plot for the IO DSCDs. Figure 6 and 7 show the MAPA calculated AODs and IO VCDs, respectively, for all the campaigns. Several datapoints are flagged as error or warnings, with a few scans giving a 'valid' flag. In the case of aerosols, the warning or error flags are mainly for scans which were during cloudy weather (Figure S5 shows the data, which were flagged as 'bad' and 'warning' along with the valid scans). As mentioned above, the cloud cover was regularly measured throughout the campaigns as a part of the meteorological observations. In addition to visual observations, we also computed the cloud index following past works based on MAX-DOAS observations (Mahajan et al., 2012; Wagner et al., 2014), which confirmed that the error and warning flags were during cloud cover periods. For the valid scans, the aerosol optical depth (AOD) ranged between 0.002 and 0.016, with a mean value of 0.003 for ISEA-34 at Bharati; between 0.001 and 0.067, with a mean value of 0.011 for ISEA-34 at Maitri; between 0.001 and 1.866, with a mean value of 0.037 for ISEA-35 at Bharati; and between 0.001 and 0.878, with a mean value of 0.016 for ISEA-36 at Bharati (Figure 6). The low values are expected considering the pristine conditions in Antarctica, although during a couple of scans elevated levels were

12

261 observed as demonstrated by the maximum value during ISEA-35 and ISEA-36. In the case of IO,

262 there were far fewer valid retrieved profiles as can be seen in Figure 7 (Figure S6 shows the all

263 scans, including the 'bad' and 'warning'). Only 343 valid total scans were retrieved for the vertical

264 profiles of IO. One of the main reasons is that for most of the scans the IO DSCDs at higher

265 elevation angles are below the detection limit and not enough information is available for the

266 model to retrieve a valid vertical profile. In the case of IO VCDs, there were only two scans that

267 showed a valid flag over the 10-day period during the ISEA-34 campaign at Bharati due to adverse

268 weather conditions leading to mostly cloudy weather. Thus, the mean VCD value of 2.83×10^{12}

269 molecules cm^{-2}, should be treated with some caution. In Maitri during ISEA-34, the IO VCD

270 ranged between 2.37×10^{12} molecules cm^{-2} and 4.25×10^{12} molecules cm^{-2}, with a mean value of

271 $3.40 \pm 0.57 \times 10^{12}$ molecules cm^{-2}. During ISEA-35 at Bharati, which had the highest number of

272 valid scans over the four campaigns, the IO VCDs ranged between 0.01×10^{12} and 5.86×10^{12}

273 molecules cm^{-2}, with a mean value of $2.62 \pm 1.16 \times 10^{12}$ molecules cm^{-2}. During ISEA-36, the IO

274 VCDs ranged between 2.78×10^{12} molecules cm^{-2} and 4.90×10^{12} molecules cm^{-2}, with a mean value

275 of $3.92 \pm 0.79 \times 10^{12}$ molecules cm^{-2} at Bharati (Table S1).

276 In addition to the VCDs, vertical profiles of aerosols (Figure S7) and IO were estimated using

277 MAPA. Figure 8 shows the typical vertical profiles of IO mixing ratios over the four expeditions.

278 The surface mixing ratios for the valid scans across all the campaigns range between 0.2 and 1.3

279 pptv (Table S1). The surface (<30 m) concentrations observed at both Maitri and Bharati are lower

280 than observations in the Weddell Sea region, where summer time concentrations exceeding 6 pptv

281 have been reported in the past (Atkinson et al., 2012; Saiz-Lopez et al., 2007a), or at the Neumayer

282 station, where long-term zenith sky DOAS measurements of IO suggest mixing ratios as high as

283 ~10 pptv during the summer (Frieß et al., 2001). It should be noted that although elevated

284 concentrations were observed at Halley, the average summer concentration, measured only 4 m

285 above the snowpack using a Long-Path DOAS instrument, was about 3 pptv, approximately a

286 factor of three higher than the observations at Bharati and Maitri. Considering that the MAX-

287 DOAS retrieved profiles are not very sensitive to the lowermost few meters, this difference is

288 expected. This is because the source of IO is expected to be from the surface and remote sensing

289 estimates have suggested that high IO concentrations in the order of 50 ppbv are present in the

290 snow interstitial air (Frieß et al., 2010), suggesting that snowpack is indeed the source for iodine

291 compounds. If this is the case, a strong gradient would be observed considering the short lifetime

292 of IO in the atmosphere, and hence the MAX-DOAS observations would be lower than the LP-

293 DOAS observations. However, this does not explain the large difference compared to Neumayer,

294 where the estimated value was 10 pptv. Indeed, Maitri is close to Neumayer, and the reasons for

295 the large difference between the two sites remains a mystery. The observations reported in this

296 study are also similar to measurements at McMurdo Sound, near the Ross Sea, where MAX-DOAS

297 observations reported a maximum of 2.6 ± 0.1 pptv with most of the observations below 1 pptv

298 during 2006 and 2007 (Hay, 2010). It should be noted that the surface values were not highly

299 weighted by the a priori. McMurdo Sound is also located in the East Antarctic, which shows lower

300 levels of IO in the satellite estimates (Schönhardt et al., 2008) and in models (Fernandez et al.,

301 2019).

302 Vertical profiles of IO have been reported only once in the past from Antarctica. These

303 measurements were made at McMurdo Sound in East Antarctica (Hay, 2010). IO over two days in

304 2006 and 2007 show typical surface concentrations of ~1 pptv (with a maximum of 2.6 pptv),

305 decreasing to ~0.2 pptv at about 200 m. A second maximum of 0.6 pptv at ~700 m was also

306 observed, but the models do not reproduce this profile shape and the observations were subject to

14

307   large uncertainties with the vertical profile above 200 m dominated by the a priori (Hay, 2010).

308   During the four campaigns studied here, elevated concentrations, similar to the surface, were

309   usually observed until about 400 m. Above this height, there is a decrease, with the retrievals

310   reducing to below 0.1 pptv (Figure 8). Although the boundary layer height was not available for

311   most of the days, radiosonde observations (not shown) , show that the boundary layer height ranged

312   between 300-700 m. The means and their standard deviations for the lowest 400 m for the different

313   campaigns are given in Table S1. The reducing standard deviations in the profile retrieval with

314   altitude show that all the profiles which reproduce elevated IO close to the ground approach zero

315   for higher altitudes, suggesting that most of the IO is within the lower part of the troposphere.

316   However, this gradient is much more gradual than estimates predicted using the THAMO one-

317   dimensional model at Halley Bay (Saiz-Lopez et al., 2008). In most models, the assumption is that

318   the source is from the snowpack, and hence a strong decreasing gradient with altitude has been

319   predicted (Saiz-Lopez et al., 2008). The gradient of this decrease depends on the photolysis of the

320   higher oxides, and on the recycling of iodine reservoir species on aerosols, both of which have

321   uncertainties. When the gradient was estimated in 2008 (Saiz-Lopez et al., 2008), the photolysis

322   rates for the higher iodine oxides were not available but this has recently been measured in the

323   laboratory (Lewis et al., 2020) and THAMO needs to be updated accordingly. Another important

324   point to consider is that the MAX-DOAS observation-based profile retrievals typically get only a

325   couple of points of information in the boundary layer and are hence not expected to capture this

326   strong decrease.

327   **3.4 Comparison with satellite-based estimates**

328   The satellite-based vertical column densities of IO across the Weddell Sea region, and the region

329   encompassing Bharati and Maitri are shown in Figure 9. The averaged satellite based VCD

330 observations suggest that lower levels of IO are expected at both the Indian bases as compared to

331 places where ground-based observations have been reported in the past, such as Halley Bay and

332 Neumayer. The mean and standard deviation over the eight years of observations for Bharati is 0.6

333 $\pm$ 0.5 $\times 10^{12}$ molecules cm^{-2}, while for Maitri the amount is 0.5 $\pm$ 0.5 $\times 10^{12}$ molecules cm^{-2}, each

334 for the whole time series. For single months the values can be higher: the mean IO VCD for Bharati

335 is 0.8 or 0.4 $\times 10^{12}$ molecules cm^{-2} in December or February, respectively, and 0.6 $\times 10^{12}$ molecules

336 cm^{-2} in March for Maitri. This is lower than mean value of 2.62 $\pm$ 1.16$\times 10^{12}$ molecules cm^{-2}

337 observed at Bharati during ISEA-35, which was the longest dataset available in this study which

338 suggests that the ground-based instruments observe larger VCDs as compared to the satellite based

339 instruments. However, it should be noted that the SCIAMACHY data is an average over all the

340 seasons, and individual daily datapoints as high as 2.1$\times 10^{12}$ molecules cm^{-2} have been observed.

341 Figure 10 shows the timeseries for Bharati and Maitri with daily averages (red dots) as well as

342 monthly averages (blue triangles) for the years 2004 to 2011. Satellite measurements from within

343 500 km around the stations were included in the analysis. It should be mentioned that this spatial

344 averaging could cause introduction of larger uncertainties due to the heterogeneity in the IO

345 distribution, but are necessary to improve the signal to noise.

346 When the whole IO column is constrained to the lower 400 m, the satellite retrieved VCDs translate

347 to a range between 0.6 – 1.3 pptv. The daily satellite VCDs tend to exceed these averaged values

348 and result in mixing ratios as high as 2 pptv. This is similar to the range observed through the four

349 campaigns reported here. However, observations during the spring time were not made over these

350 four campaigns, when emissions of iodine species have been shown to peak at Halley Bay (Saiz-

351 Lopez et al., 2007a). During the spring season, values as high as 20 pptv was observed at Halley

352 Bay, a factor of ten higher than during the summer at the Indian stations. However, the satellite

16

353   observations do not show a large peak over the springtime over both Indian stations. Another

354   outstanding question is whether the satellites are sensitive to the lower 100-200 m, considering the

355   strong gradient in IO. Figure S8 shows the block AMFs for satellite retrievals showing a significant

356   difference between the block AMFs over Antarctica at different albedo values. Over the ice-

357   covered regions in Antarctica, the satellite is sensitive to the lower troposphere as the albedo is

358   usually 0.9 or above. Observations have shown that open water has an albedo of 0.05–0.2 (Jin et

359   al., 2004), whereas the albedo of sea ice ranges between 0.6 and 0.7 for bare ice and 0.8–0.9 for

360   snow-covered ice (Perovich et al., 2002). In the case of Bharati, the Quilty Bay is not ice covered

361   during the summer and hence along the light path in Bharati, the sensitivity of the satellite is much

362   lower. Use of a higher albedo would result in an underestimation of the VCD by the satellite, which

363   is the case when compared to the ground-based instruments. At Mairti this should not be the case

364   considering that Maitri is 125 km inland from the coast, and the ice shelf is less than 1 km from

365   the station along the light path. It should be noted that the MAPA LUTs are calculated for a low

366   surface albedo (5%) and hence, at least for some of the measurements, the surface albedo is

367   probably much higher, especially at Maitri. As far as we understand, the effect of the surface

368   albedo mainly cancels out in the MAX-DOAS analysis, but it could be one possible uncertainty

369   on the retrieval results. Another reason for the discrepancy between the ground based and satellite

370   retrieved VCDs could be the overpass time, which was approximately 09:00 am local time.

371   Although this should not be a large factor during the summer months due to long sunlit hours, and

372   that the numbers given above were averages through the entire campaign for the ground-based

373   observations, measurements at Halley Bay have shown a strong diurnal profile peaking at noon

374   (Saiz-Lopez et al., 2007a). Hence, it is possible that the ground-based observations, which are

375   filtered for SZA>75°, capture higher values than the satellite.

376   Finally, a point to consider is that the satellite data available from SCIAMACHY is for the period

377   of 2004-2011, whereas the MAX-DOAS observations were conducted over three summers from

378   2015. This temporal discrepancy, although small considering the long satellite dataset, could

379   contribute to the difference in the retrieved VCDs. Recent observations of iodine in ice-cores in

380   the Alpine region and over Greenland have shown an increasing trend for atmospheric iodine in

381   the northern hemisphere (Cuevas et al., 2018; Legrand et al., 2018). In the Antarctic only seasonal

382   and geographical variations in halogens in the ice have been studied and no long term dataset is

383   available (Vallelonga et al., 2017). The main cause for this increase is suggested to be an increase

384   in tropospheric ozone, which drives the emission of iodine compounds from the ocean surface

385   through heterogenous chemistry at the ocean interstitial surface (Carpenter et al., 2013). Although

386   questions regarding the strength of this inorganic source in affecting IO concentrations in the

387   Southern Ocean remain (Inamdar et al., 2020; Mahajan et al., 2019), it is possible that the

388   discrepancy between the satellite and ground based data is because of a different time period.

389   However, no increasing trend was observed in the satellite data for the period between 2004-2011

390   (Figure 10), which suggests that a factor of three increase in the VCDs is most likely due to a

391   difference in the measurement technique and sensitivities rather than a change in the emissions.

392

393   **3.5 Airmass origin dependence**

394   Year-long observations at Halley Bay in West Antarctica, which were made using the LP-DOAS

395   instrument, suggested a oceanic primary source (Saiz-Lopez et al., 2007a). The authors showed

396   through the tracking of airmass back-trajectories, which displayed that elevated levels of IO were

397   present in airmasses that passed over the coastal and oceanic regions compared to the airmasses

18

398   that had only continental exposures. However, even in airmasses that had passed only over the

399   continent for the past five days, the IO levels were still above the detection limit, which suggested

400   that even if the primary source is oceanic, a secondary source from the snow pack contributed to

401   the atmospheric IO. Indeed, subsequent studies have tried to explain the snowpack source through

402   recycling of primary emissions from the ocean (Fernandez et al., 2019) and one study has even

403   suggested a strong snowpack source based on simulated observations (Frieß et al., 2010). Although

404   the levels of IO are much lower than the peak concentrations seen at Halley Bay, we studied the

405   back-trajectories to see if the origin of airmasses lead to a difference in the observed IO levels at

406   both Bharati and Maitri. Considering the short lifetime of reactive iodine compounds in the

407   atmosphere, we calculated the exposure of each HYSPLIT calculated back-trajectory according to

408   the region it passed over the last 12 hours. Depending on where the trajectories spend the most

409   amount of time, they were classified into coastal, continental, and oceanic airmasses. The coastal

410   region was defined as a 0.5° belt along the Antarctic coastline, with regions to the north and south

411   of this belt considered to be oceanic and continental, even though most of them had coastal origin

412   when the 5 day trajectories are considered (Figure S9). Using the profiles which were valid, no

413   clear dependence on the airmass origin was observed. Indeed, most of the data points at both

414   stations corresponded to airmasses which were either coastal or continental (Figure S10) and is

415   representative of the typical wind patterns during the summer season. Thus, using this dataset, it

416   was not possible to draw any conclusions regarding the possible sources of IO in this region, and

417   a longer study is needed in the future.

418

419   **4. Conclusions**

420   This study presents observations of iodine oxide (IO) at the Indian Antarctic bases Maitri and

421   Bharati made over three summers from 2015 through 2017. IO was observed intermittently during

422   all the campaigns, with mixing ratios below 2 pptv. Using a profile retrieval algorithm, vertical

423   gradients of IO were estimated, and these showed a decreasing profile with a peak in the boundary

424   layer. The vertical profiles confirmed past hypothesis of a source from the ground considering a

425   sharp gradient. The vertical columns observed using the ground-based instrument are

426   approximately a factor of three-five higher than the climatological mean observed by the satellite,

427   which could be due to a difference in the measurement techniques and sensitivities. Airmass origin

428   analysis using back-trajectories did not lead to a conclusive answer about the source regions.

429   Indeed, it raises new questions on comparison with past observations, which show that we still do

430   not understand iodine chemistry in the polar regions. This study suggests that a longer dataset over

431   different seasons and regions of Antarctica is necessary to answer the outstanding questions

432   regarding the sources and seasonal importance of IO in the Indian Ocean sector of Antarctica.

433

439   **6. Author contributions:**

ASM conceptualised the research plan and methodology, did the analysis and wrote the

manuscript. MSB did the field observations. SB, TW, NB and ASL helped with the interpretation

of the observations and AS provided the satellite observations and helped interpret them.

7. References

Allan, J. D., Williams, P. I., Najera, J., Whitehead, J. D., Flynn, M. J., Taylor, J. W., Liu, D.,

Darbyshire, E., Carpenter, L. J., Chance, R., Andrews, S. J., Hackenberg, S. C. and McFiggans,

G.: Iodine observed in new particle formation events in the Arctic atmosphere during

ACCACIA, Atmos. Chem. Phys., 15(10), 5599–5609, doi:10.5194/acp-15-5599-2015, 2015.

Atkinson, H. M., Huang, R.-J., Chance, R., Roscoe, H. K., Hughes, C., Davison, B., Schönhardt,

A., Mahajan, A. S., Saiz-Lopez, A., Hoffmann, T. and Liss, P. S.: Iodine emissions from the sea

ice of the Weddell Sea, Atmos. Chem. Phys., 12, 11229–11244, doi:10.5194/acp-12-11229-

2012, 2012.

Barrie, L. A., Bottenheim, J. W., Schnell, R. C., Crutzen, P. J. and Rasmussen, R. A.: Ozone

destruction and photochemical reactions at polar sunrise in the lower Arctic atmosphere, Nature,

334(14), 138–141 [online] Available from:

http://www.nature.com/nature/journal/v334/n6178/abs/334138a0.html (Accessed 3 May 2012),

1988.

Beirle, S., Dörner, S., Donner, S., Remmers, J., Wang, Y. and Wagner, T.: The Mainz Profile

Algorithm (MAPA), Atmos. Meas. Tech. Discuss., 1–33, doi:10.5194/amt-2018-375, 2018.

Bogumil, K., Orphal, J., Homann, T., Voigt, S., Spietz, P., Fleischmann, O. C., Vogel, A.,

461   Hartmann, M., Kromminga, H., Bovensmann, H., Frerick, J. and Burrows, J. P.: Measurements

462   of molecular absorption spectra with the SCIAMACHY pre-flight model: instrument

463   characterization and reference data for atmospheric remote-sensing in the 230–2380 nm region,

464   J. Photochem. Photobiol. A Chem., 157(2–3), 167–184, doi:10.1016/S1010-6030(03)00062-5,

465   2003.

466   Bottenheim, J. W., Gallant, A. G. and Brice, K. A.: Measurements of NOy Species and O3 at 82-

467   Degrees-N Latitude, Geophys. Res. Lett., 13(2), 113–116, 1986.

468   Burrows, J. P., Hölzle, E., Goede, A. P. H., Visser, H. and Fricke, W.: SCIAMACHY – Scanning

469   Imaging Absorption Spectrometer for Atmospheric Chartography, Acta Astronaut., 35, 445–451,

470   1995.

471   Buys, Z., Brough, N., Huey, L. G., Tanner, D. J., von Glasow, R. and Jones, a. E.: High

472   temporal resolution Br2, BrCl and BrO observations in coastal Antarctica, Atmos. Chem. Phys.,

473   13, 1329–1343, doi:10.5194/acp-13-1329-2013, 2013.

474   Carpenter, L. J., Wevill, D. J., Palmer, C. J. and Michels, J.: Depth profiles of volatile iodine and

475   bromine-containing halocarbons in coastal Antarctic waters, Mar. Chem., 103, 227–236, 2007.

476   Carpenter, L. J., MacDonald, S. M., Shaw, M. D., Kumar, R., Saunders, R. W., Parthipan, R.,

477   Wilson, J. and Plane, J. M. C.: Atmospheric iodine levels influenced by sea surface emissions of

478   inorganic iodine, Nat. Geosci., 6(2), 108–111, doi:10.1038/ngeo1687, 2013.

479   Chance, K. V and Spurr, R. J.: Ring effect studies: Rayleigh scattering, including molecular

480   parameters for rotational Raman scattering, and the Fraunhofer spectrum., Appl. Opt., 36(21),

481   5224–5230 [online] Available from: http://www.ncbi.nlm.nih.gov/pubmed/18259337, 1997.

482   Cuevas, C. A., Maffezzoli, N., Corella, J. P., Spolaor, A., Vallelonga, P., Kjær, H. A., Simonsen,

483   M., Winstrup, M., Vinther, B., Horvat, C., Fernandez, R. P., Kinnison, D., Lamarque, J.-F.,

484   Barbante, C. and Saiz-Lopez, A.: Rapid increase in atmospheric iodine levels in the North

485   Atlantic since the mid-20th century, Nat. Commun., 9(1), 1452, doi:10.1038/s41467-018-03756-

486   1, 2018.

487   Deutschmann, T., Beirle, S., Frieß, U., Grzegorski, M., Kern, C., Kritten, L., Platt, U., Prados-

488   Román, C., Pukite, J., Wagner, T., Werner, B. and Pfeilsticker, K.: The Monte Carlo atmospheric

489   radiative transfer model McArtim: Introduction and validation of Jacobians and 3D features, J.

490   Quant. Spectrosc. Radiat. Transf., 112(6), 1119–1137, doi:10.1016/j.jqsrt.2010.12.009, 2011.

491   Draxler, R. and Rolph, G.: HYSPLIT (HYbrid Single Particle Lagrangian Integrated Tra-

492   jectory). Model access via NOAA ARL Ready, [online] Available from:

493   http://www.arl.noaa.gov/ready/ hysplit4.html, 2003.

494   Fayt, C. and Van Roozendael, M.: QDOAS 1.00. Software User Manual, [online] Available

495   from: http://uv-vis.aeronomie.be/software/QDOAS/, 2013.

496   Fernandez, R. P., Carmona-Balea, A., Cuevas, C. A., Barrera, J. A., Kinnison, D. E., Lamarque,

497   J., Blaszczak-Boxe, C., Kim, K., Choi, W., Hay, T., Blechschmidt, A., Schönhardt, A., Burrows,

498   J. P. and Saiz-Lopez, A.: Modeling the Sources and Chemistry of Polar Tropospheric Halogens

499   (Cl, Br, and I) Using the CAM-Chem Global Chemistry-Climate Model, J. Adv. Model. Earth

500   Syst., 11(7), 2259–2289, doi:10.1029/2019MS001655, 2019.

501   Fogelqvist, E. and Tanhua, T.: Iodinated C1-C4 hydrocarbons released from ice algae in

502   Antarctica BT - Naturally-Produced Organohalogens, edited by A. Grimvall and E. W. B. de

503   Leer, pp. 295–305, Springer Netherlands, Dordrecht., 1995.

23

504   Frieß, U., Wagner, T., Pundt, I., Pfeilsticker, K., Platt, U. and Friefi, U.: Spectroscopic

505   Measurements of Tropospheric Iodine Oxide at Neumayer Station, Antarctica, Geophys. Res.

506   Lett., 28(10), 1941–1944, 2001.

507   Frieß, U., Deutschmann, T., Gilfedder, B. S., Weller, R. and Platt, U.: Iodine monoxide in the

508   Antarctic snowpack, Atmos. Chem. Phys., 10(5), 2439–2456 [online] Available from:

509   http://www.atmos-chem-phys.net/10/2439/2010/, 2010.

510   Garrison, D. L. and Buck, K. R.: The biota of Antarctic pack ice in the Weddell sea and

511   Antarctic Peninsula regions, Polar Biol., 10(3), 211–219, doi:10.1007/BF00238497, 1989.

512   Gómez Martín, J. C., Spietz, P. and Burrows, J. P.: Spectroscopic studies of the I-2/O-3

513   photochemistry - Part 1: Determination of the absolute absorption cross sections of iodine oxides

514   of atmospheric relevance, J. Photochem. Photobiol. A - Chem., 176(1–3), 15–38,

515   doi:10.1016/j.jphotochem.2005.09.024, 2005.

516   Grilli, R., Legrand, M., Kukui, A., Méjean, G., Preunkert, S. and Romanini, D.: First

517   investigations of IO, BrO, and NO2 summer atmospheric levels at a coastal East Antarctic site

518   using mode-locked cavity enhanced absorption spectroscopy., Geophys. Res. Lett., 40(4), 791–

519   796, doi:10.1002/GRL.50154, 2013.

520   Hay, T.: MAX – DOAS measurements of bromine explosion events in McMurdo Sound ,

521   Antarctica, University of Canterbury., 2010.

522   Hollwedel, J., Wenig, M., Beirle, S., Kraus, S., Kühl, S., Wilms-Grabe, W., Platt, U. and

523   Wagner, T.: Year-to- Year Variability of Polar Tropospheric BrO as seen by GOME, Adv. Sp.

524   Res., 34, 804–808 [online] Available from: http://dx.doi.org/10.1016/j.asr.2003.08.060, 2004.

525   Hönninger, G., von Friedeburg, C. and Platt, U.: Multi axis differential optical absorption

526   spectroscopy (MAX-DOAS), Atmos. Chem. Phys., 4, 231–254, doi:10.5194/acp-4-231-2004,

527   2004.

528   Inamdar, S., Tinel, L., Chance, R., Carpenter, L. J., Sabu, P., Chacko, R., Tripathy, S. C., Kerkar,

529   A. U., Sinha, A. K., Bhaskar, P. V., Sarkar, A., Roy, R., Sherwen, T. T., Cuevas, C., Saiz-Lopez,

530   A., Ram, K. and Mahajan, A. S.: Estimation of Reactive Inorganic Iodine Fluxes in the Indian

531   and Southern Ocean Marine Boundary Layer, Atmos. Chem. Phys., 20(20), 12093–12114,

532   doi:10.5194/acp-20-12093-2020, 2020.

533   Jin, Z., Charlock, T. P., Smith, W. L. and Rutledge, K.: A parameterization of ocean surface

534   albedo, Geophys. Res. Lett., 31(22), 1–4, doi:10.1029/2004GL021180, 2004.

535   Koenig, T. K., Baidar, S., Campuzano-Jost, P., Cuevas, C. A., Dix, B., Fernandez, R. P., Guo,

536   H., Hall, S. R., Kinnison, D., Nault, B. A., Ullmann, K., Jimenez, J. L., Saiz-Lopez, A. and

537   Volkamer, R.: Quantitative detection of iodine in the stratosphere, Proc. Natl. Acad. Sci., (15),

538   201916828, doi:10.1073/pnas.1916828117, 2020.

539   Kreher, K., Johnston, P. V., Wood, S. W., Nardi, B. and Platt, U.: Ground-based measurements

540   of tropospheric and stratospheric BrO at Arrival Heights, Antarctica, Geophys. Res. Lett.,

541   24(23), 3021–3024, doi:10.1029/97GL02997, 1997.

542   Legrand, M., McConnell, J. R., Preunkert, S., Arienzo, M., Chellman, N., Gleason, K., Sherwen,

543   T., Evans, M. J. and Carpenter, L. J.: Alpine ice evidence of a three-fold increase in atmospheric

544   iodine deposition since 1950 in Europe due to increasing oceanic emissions, Proc. Natl. Acad.

545   Sci., 115(48), 12136–12141, doi:10.1073/pnas.1809867115, 2018.

546 Lewis, T. R., Gómez Martín, J. C., Blitz, M. A., Cuevas, C. A., Plane, J. M. C. and Saiz-Lopez,

547 A.: Determination of the absorption cross sections of higher-order iodine oxides at 355 and 532

548 nm, Atmos. Chem. Phys., 20(18), 10865–10887, doi:10.5194/acp-20-10865-2020, 2020.

549 Mahajan, A. S., Shaw, M., Oetjen, H., Hornsby, K. E., Carpenter, L. J., Kaleschke, L., Tian-

550 Kunze, X., Lee, J. D., Moller, S. J., Edwards, P. M., Commane, R., Ingham, T., Heard, D. E. and

551 Plane, J. M. C.: Evidence of reactive iodine chemistry in the Arctic boundary layer, J. Geophys.

552 Res., 115(D20303,), doi:dx.doi.org/10.1029/2009JD013665, 2010.

553 Mahajan, A. S., Gómez Martín, J. C., Hay, T. D., Royer, S.-J., Yvon-Lewis, S. A., Liu, Y., Hu,

554 L., Prados-Román, C., Ordóñez, C., Plane, J. M. C. and Saiz-Lopez, A.: Latitudinal distribution

555 of reactive iodine in the Eastern Pacific and its link to open ocean sources, Atmos. Chem. Phys.,

556 12, 11609–11617, doi:10.5194/acp-12-11609-2012, 2012.

557 Mahajan, A. S., Tinel, L., Hulswar, S., Cuevas, C. A., Wang, S., Ghude, S., Naik, R. K., Mishra,

558 R. K., Sabu, P., Sarkar, A., Anilkumar, N. and Saiz Lopez, A.: Observations of iodine oxide in

559 the Indian Ocean marine boundary layer: A transect from the tropics to the high latitudes, Atmos.

560 Environ. X, 1, 100016, doi:10.1016/j.aeaoa.2019.100016, 2019.

561 Meller, R. and Moortgat, G. K.: Temperature dependence of the absorption cross sections of

562 formaldehyde between 223 and 323 K in the wavelength range 225-375 nm, J. Geophys. Res.,

563 105(D6), 7089–7101 [online] Available from: http://dx.doi.org/10.1029/1999JD901074, 2000.

564 O'Dowd, C. D., Facchini, M. C., Cavalli, F., Ceburnis, D., Mircea, M., Decesari, S., Fuzzi, S.,

565 Yoon, Y. J., Putaud, J. P. and Dowd, C. D. O.: Biogenically driven organic contribution to

566 marine aerosol, Nature, 431(7009), 676–680, doi:10.1038/nature02970.1., 2004.

567 Oltmans, S. J. and Komhyr, W. D.: Surface Ozone Distributions and Variations from 1973-1984

568 Measurements at the Noaa Geophysical Monitoring for Climatic-Change Base-Line

569 Observatories, J. Geophys. Res. - Atmos., 91(D4), 5229–5236, 1986.

570 Perovich, D. K., Grenfell, T. C., Light, B. and Hobbs, P. V.: Seasonal evolution of the albedo of

571 multiyear Actic sea ice, J. Geophys. Res. C Ocean., 107(10), doi:10.1029/2000jc000438, 2002.

572 Platt, U. and Stutz, J.: Differential optical absorption spectroscopy: Principles and applications,

573 First Edit., Springer., 2008.

574 Prakash Chaubey, J., Krishna Moorthy, K., Suresh Babu, S. and S. Nair, V.: The optical and

575 physical properties of atmospheric aerosols over the Indian Antarctic stations during southern

576 hemispheric summer of the International Polar Year 2007ĝ€"2008, Ann. Geophys., 29(1), 109–

577 121, doi:10.5194/angeo-29-109-2011, 2011.

578 Raso, A. R. W., Custard, K. D., May, N. W., Tanner, D., Newburn, M. K., Walker, L., Moore, R.

579 J., Huey, L. G., Alexander, L., Shepson, P. B. and Pratt, K. A.: Active molecular iodine

580 photochemistry in the Arctic, Proc. Natl. Acad. Sci. U. S. A., 114(38), 10053–10058,

581 doi:10.1073/pnas.1702803114, 2017.

582 Reifenhäuser, W. and Heumann, K. G.: Determinations of methyl-iodine in the antarctic

583 atmosphere at the south polar sea, Atmos. Environ. Part a-General Top., 26(16), 2905–2912,

584 1992.

585 Richter, A., Wittrock, F., Ladstätter-Weißenmayer, A. and Burrows, J. P.: GOME measurements

586 of stratospheric and tropospheric BrO, Adv. Sp. Res., 29(11), 1667–1672, 2002.

587 Rothman, L. S., Gordon, I. E., Babikov, Y., Barbe, A., Chris Benner, D., Bernath, P. F., Birk,

27

588   M., Bizzocchi, L., Boudon, V., Brown, L. R., Campargue, A., Chance, K., Cohen, E. a., Coudert,

589   L. H., Devi, V. M., Drouin, B. J., Fayt, A., Flaud, J.-M., Gamache, R. R., Harrison, J. J.,

590   Hartmann, J.-M., Hill, C., Hodges, J. T., Jacquemart, D., Jolly, A., Lamouroux, J., Le Roy, R. J.,

591   Li, G., Long, D. a., Lyulin, O. M., Mackie, C. J., Massie, S. T., Mikhailenko, S., Müller, H. S. P.,

592   Naumenko, O. V., Nikitin, A. V., Orphal, J., Perevalov, V., Perrin, A., Polovtseva, E. R.,

593   Richard, C., Smith, M. a. H., Starikova, E., Sung, K., Tashkun, S., Tennyson, J., Toon, G. C.,

594   Tyuterev, V. G. and Wagner, G.: The HITRAN 2012 molecular spectroscopic database, J. Quant.

595   Spectrosc. Radiat. Transf., 130, 4–50, doi:10.1016/j.jqsrt.2013.07.002, 2013.

596   Saiz-Lopez, A. and Blaszczak-boxe, C. S.: The polar iodine paradox, Atmos. Environ., 145, 72–

597   73, doi:10.1016/j.atmosenv.2016.09.019, 2016.

598   Saiz-Lopez, A. and von Glasow, R.: Reactive halogen chemistry in the troposphere., Chem. Soc.

599   Rev., doi:10.1039/c2cs35208g, 2012.

600   Saiz-Lopez, A., Mahajan, A. S., Salmon, R. A., Bauguitte, S. J.-B., Jones, A. E., Roscoe, H. K.

601   and Plane, J. M. C.: Boundary Layer Halogens in Coastal Antarctica, Science (80-.)., 317(5836),

602   348–351, doi:10.1126/science.1141408, 2007a.

603   Saiz-Lopez, A., Chance, K. V., Liu, X., Kurosu, T. P. and Sander, S. P.: First observations of

604   iodine oxide from space, Geophys. Res. Lett., 34(12), L12812, doi:10.1029/2007GL030111,

605   2007b.

606   Saiz-Lopez, A., Plane, J. M. C., Mahajan, A. S., Anderson, P. S., Bauguitte, S. J.-B., Jones, A.

607   E., Roscoe, H. K., Salmon, R. A., Bloss, W. J., Lee, J. D. and Heard, D. E.: On the vertical

608   distribution of boundary layer halogens over coastal Antarctica: implications for O-3, HOx, NOx

609   and the Hg lifetime, Atmos. Chem. Phys., 8(4), 887–900, 2008.

28

610   Saiz-Lopez, A., Plane, J. M. C., Baker, A. R., Carpenter, L. J., von Glasow, R., Martín, J. C. G.,

611   McFiggans, G. B., Saunders, R. W. and Gómez Martín, J. C.: Atmospheric Chemistry of Iodine,

612   Chem. Rev., 112(3), 1773–1804, doi:10.1021/cr200029u, 2012.

613   Saiz-Lopez, A., Blaszczak-Boxe, C. S. and Carpenter, L. J.: A mechanism for biologically-

614   induced iodine emissions from sea-ice, Atmos. Chem. Phys., 15, 9731–9746, doi::10.5194/acp-

615   15-9731-2015, 2015a.

616   Saiz-Lopez, A., Baidar, S., Cuevas, C. A., Koenig, T. K., Fernandez, R. P., Dix, B., Kinnison, D.

617   E., Lamarque, J., Rodriguez-Lloveras, X., Campos, T. L. and Volkamer, R.: Injection of iodine

618   to the stratosphere, Geophys. Res. Lett., 42, 6852–6859, doi:10.1002/2015GL064796, 2015b.

619   Schönhardt, A., Richter, A., Wittrock, F., Kirk, H., Oetjen, H., Roscoe, H. K. and Burrows, J. P.:

620   Observations of iodine monoxide (IO) columns from satellite, Atmos. Chem. Phys., 8, 637–653

621   [online] Available from: http://hal-insu.archives-ouvertes.fr/hal-00296438/ (Accessed 30 April

622   2012), 2008.

623   Schönhardt, A., Begoin, M., Richter, a., Wittrock, F., Kaleschke, L., Gómez Martín, J. C. and

624   Burrows, J. P.: Simultaneous satellite observations of IO and BrO over Antarctica, Atmos.

625   Chem. Phys., 12(14), 6565–6580, doi:10.5194/acp-12-6565-2012, 2012.

626   Stutz, J., Kim, E. S., Platt, U., Bruno, P., Perrino, C. and Febo, A.: UV-visible absorption cross

627   sections of nitrous acid, J. Geophys. Res., 105(D11), 14585–14592, 2000.

628   Thalman, R. and Volkamer, R. A.: Temperature Dependent Absorption Cross-Sections of O2-O2

629   collision pairs between 340 and 630 nm and at atmospherically relevant pressure, Phys. Chem.

630   Chem. Phys., 15, 15371–15381, doi:10.1039/C3CP50968K, 2013.

631   Theys, N., Van Roozendael, M., Hendrick, F., Yang, X., De Smedt, I., Richter, A., Begoin, M.,

632   Errera, Q., Johnston, P. V., Kreher, K. and De Mazière, M.: Global observations of tropospheric

633   BrO columns using GOME-2 satellite data, Atmos. Chem. Phys., 11, 1791–1811,

634   doi:10.5194/acp-11-1791-2011, 2011.

635   Tuckermann, M., Ackermann, R., Golz, C., LorenzenSchmidt, H., Senne, T., Stutz, J., Trost, B.,

636   Unold, W., Platt, U. and Lorenzen-Schmidt, H.: DOAS-observation of halogen radical-catalysed

637   arctic boundary layer ozone destruction during the ARCTOC-campaigns 1995 and 1996 in Ny-

638   Alesund, Spitsbergen, Tellus B, 49B(5), 533–555, 1997.

639   Vallelonga, P., Maffezzoli, N., Moy, A. D., Curran, M. A. J., Vance, T. R., Edwards, R., Hughes,

640   G., Barker, E., Spreen, G., Saiz-Lopez, A., Corella, J. P., Cuevas, C. A. and Spolaor, A.: Sea-ice-

641   related halogen enrichment at Law Dome, coastal East Antarctica, Clim. Past, 13(2), 171–184,

642   doi:10.5194/cp-13-171-2017, 2017.

643   Vandaele, A. C., Hermans, C., Simon, P. C., Carleer, M., Colin, R., Fally, S., Merienne, M. F.,

644   Jenouvrier, A. and Coquartii, B.: Measurements od the NO2 absorption cross-section from 42000

645   cm-1 to 10000 cm-1 (238-1000 nm) at 220 K and 294 K, J. Quant. Spectrosc. Radiat. Transf.,

646   59(3), 171–184, 1998a.

647   Vandaele, A. C., Hermans, C., Simon, P., Carleer, M. R., Colins, R., Fally, F., Merienne, M. F.,

648   Jenouvrier, A. and Coquart, B.: Measurements of NO2 absorption cross-sections at 42000 cm-1

649   to 10000 cm-1 (238-1000 nm) at 220 K and 294 K, J. Quant. Spectrosc. Radiat. Transf., 59(3–5),

650   171–184, 1998b.

651   Wagner, T., Leue, C., Wenig, M., Pfeilsticker, K. and Platt, U.: Spatial and temporal distribution

652   of enhanced boundary layer BrO concentrations measured by the GOME instrument aboard

653   ERS-2, J. Geophys. Res. - Atmos., 106(D20), 24225–24235, 2001.

654   Wagner, T., Dix, B., Friedeburg, C. V., Frieß, U., Sanghavi, S., Sinreich, R. and Platt, U.: MAX-

655   DOAS O 4 measurements: A new technique to derive information on atmospheric aerosols—

656   Principles and information content, J. Geophys. Res., 109(D22), doi:10.1029/2004JD004904,

657   2004.

658   Wagner, T., Beirle, S. and Deutschmann, T.: Three-dimensional simulation of the Ring effect in

659   observations of scattered sun light using Monte Carlo radiative transfer models, Atmos. Meas.

660   Tech., 2(1), 113–124, doi:10.5194/amt-2-113-2009, 2009.

661   Wagner, T., Apituley, A., Beirle, S., Dörner, S., Friess, U., Remmers, J. and Shaiganfar, R.:

662   Cloud detection and classification based on MAX-DOAS observations, Atmos. Meas. Tech.,

663   7(5), 1289–1320, doi:10.5194/amt-7-1289-2014, 2014.

664   Wagner, T., Beirle, S., Benavent, N., Bösch, T., Chan, K. L., Donner, S., Dörner, S., Fayt, C.,

665   Frieß, U., García-Nieto, D., Gielen, C., González-Bartolome, D., Gomez, L., Hendrick, F.,

666   Henzing, B., Jin, J. L., Lampel, J., Ma, J., Mies, K., Navarro, M., Peters, E., Pinardi, G.,

667   Puentedura, O., Puķīte, J., Remmers, J., Richter, A., Saiz-Lopez, A., Shaiganfar, R., Sihler, H.,

668   Van Roozendael, M., Wang, Y. and Yela, M.: Is a scaling factor required to obtain closure

669   between measured and modelled atmospheric O&lt;sub&gt;4&lt;/sub&gt;

670   absorptions? An assessment of uncertainties of measurements and radiative transfer simulations

671   for 2 selected days during th, Atmos. Meas. Tech., 12(5), 2745–2817, doi:10.5194/amt-12-2745-

672   2019, 2019.

673

674

675 Figures
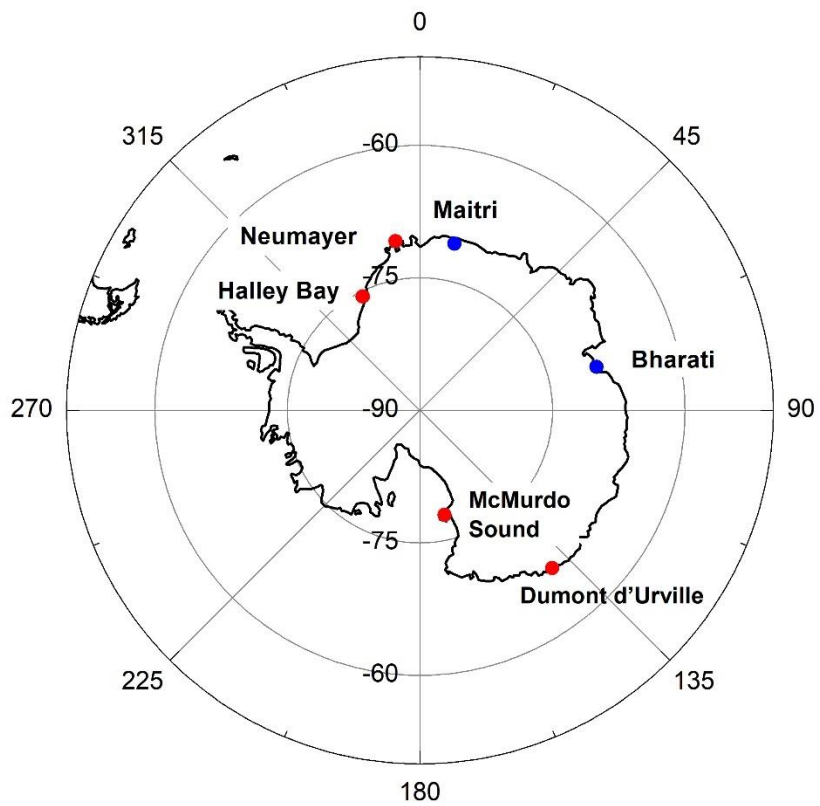
676

677 **Figure 1:** Map showing the location of the two Indian Antarctic stations, Maitri and Bharati, where

678 observations of IO were performed during this study (blue dots). Previous locations that have

679 reported observations of IO (Frieß et al., 2001; Grilli et al., 2013; Hay, 2010; Saiz-Lopez et al.,

680 2007a) are also marked on the map (red dots).

681
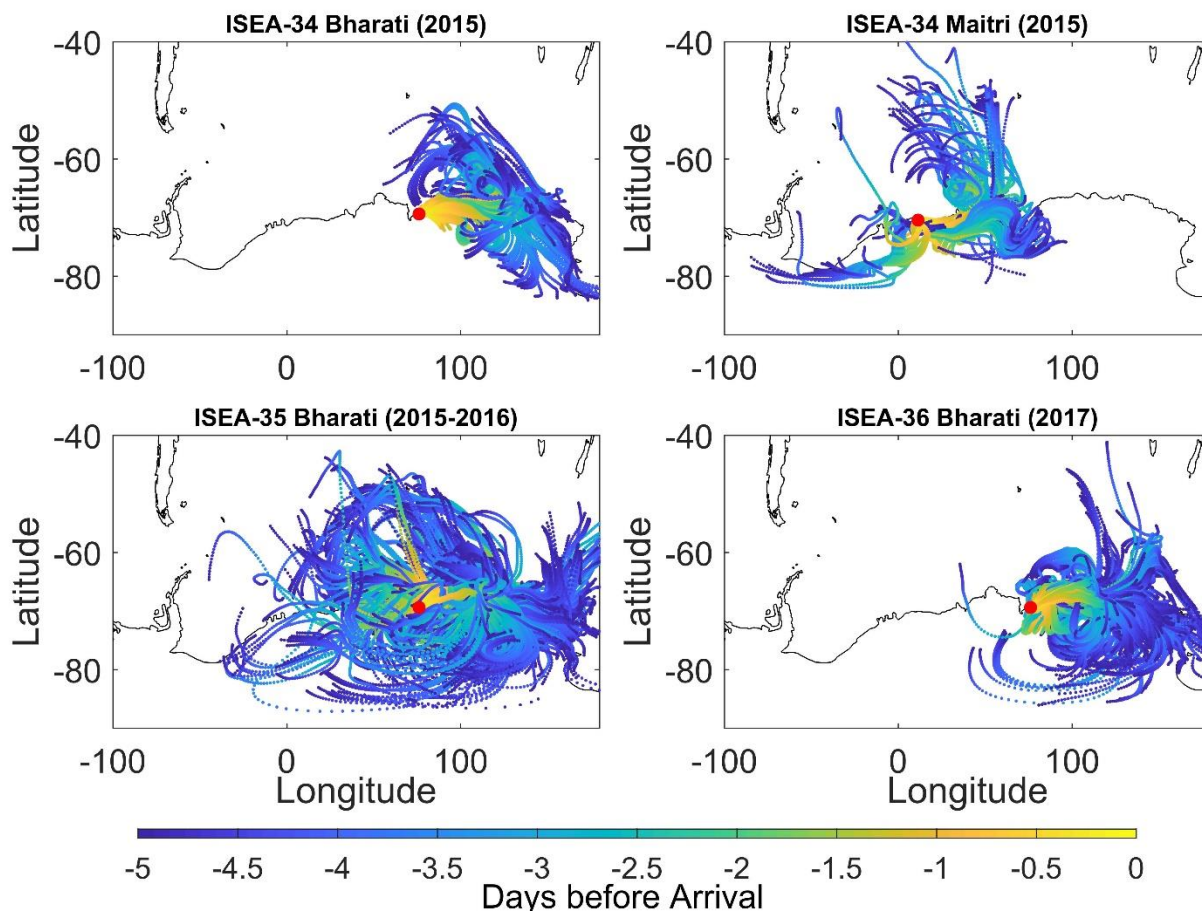
33

Figure 2: 5-day back-trajectories arriving at the two stations on the days that the measurements of IO were conducted as a part of the 34th, 35th and 36th ISEA expeditions are shown. The back-trajectories were calculated using the HYbrid Single-Particle Lagrangian Integrated Trajectory (HYSPLIT) model, arriving every hour (Draxler and Rolph, 2003).
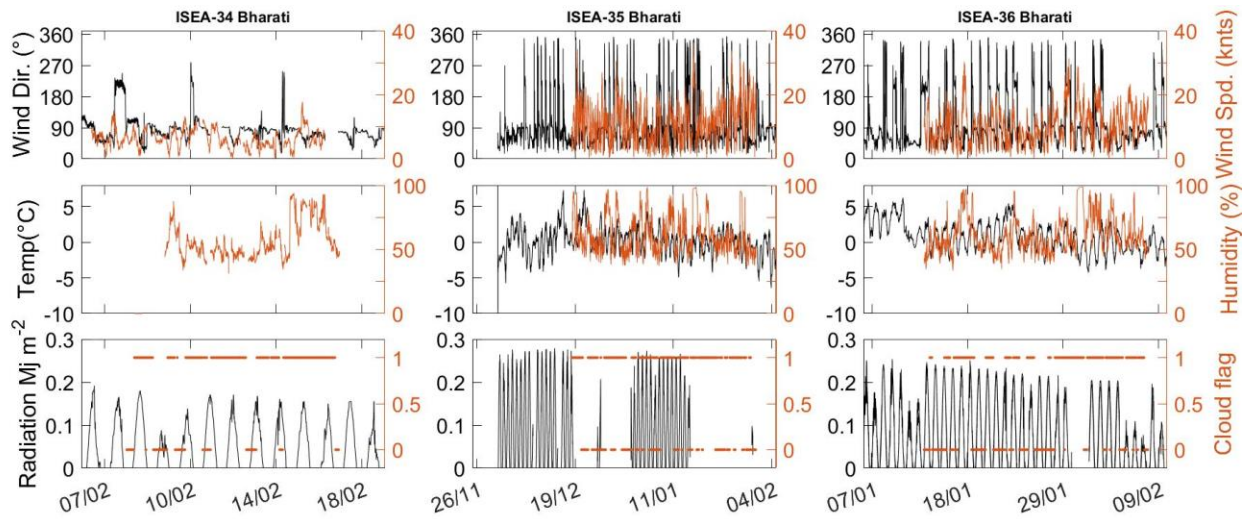
Figure 3: Observations of different meteorological parameters that were measured during the various summer campaigns are shown here. The top panels show the wind direction and speed; the middle panels show the temperature and humidity; and the bottom panels show the radiation and cloudiness (1 is defined as 30% cloudy skies and above). Observations of these parameters were not made during the 34th ISEA at Maitri and the gaps indicate instrumental or observational issues. The data had a time resolution of 5 min. The times are in UTC.

696
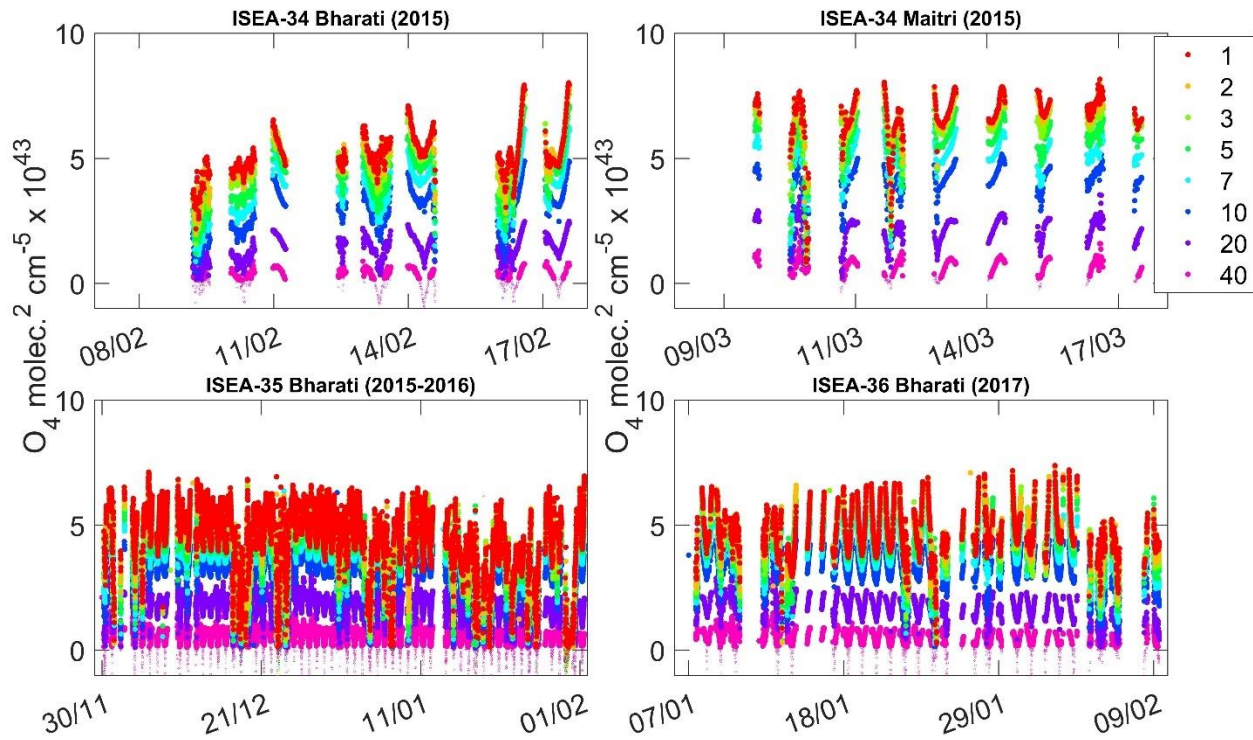
Figure 4: O$_4$ DSCDs observed during the four campaigns are shown. The empty circles represent

values below the 2σ detection limit of the instrument, while the filled circles are values above the

2σ detection limit. The data are color-coded according to elevation angles. The times are in UTC.

700
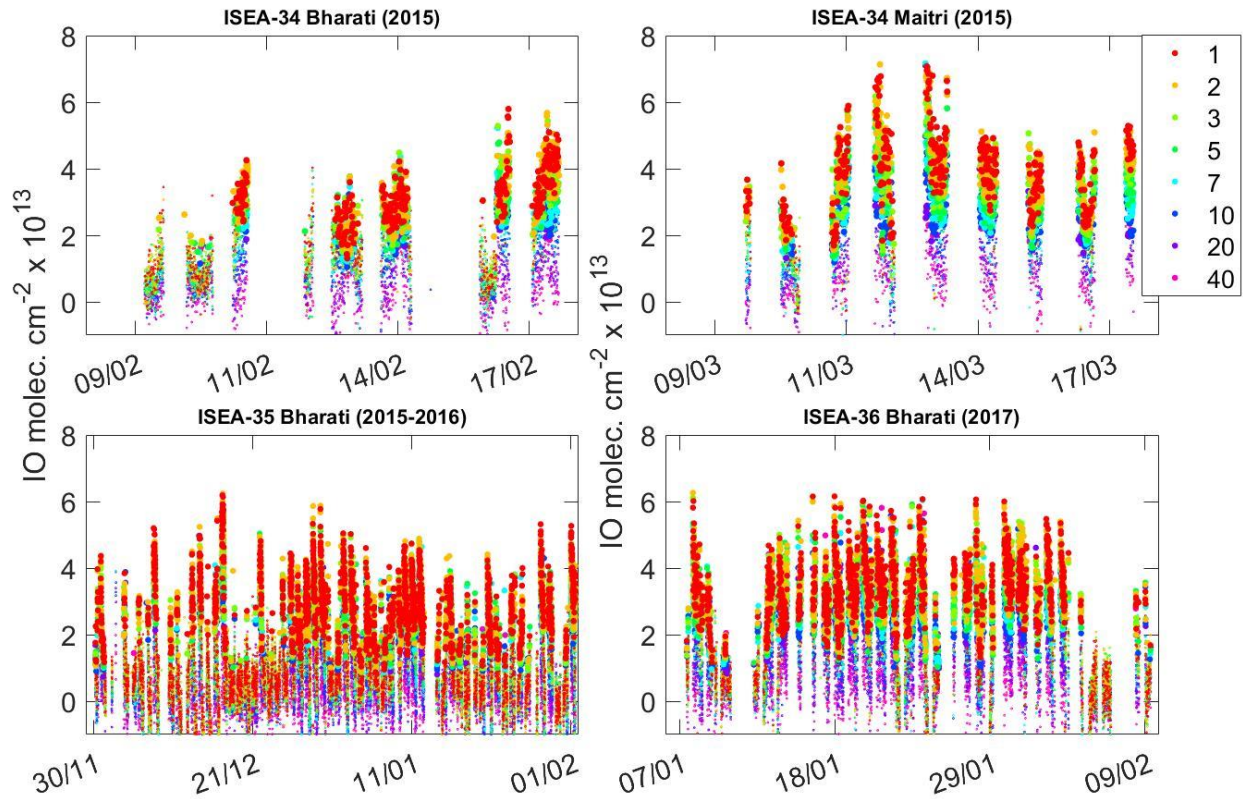
Figure 5: IO DSCDs observed during the four campaigns are shown. The smaller circles represent values below the 2σ detection limit of the instrument, while the bigger circles are values above the 2σ detection limit. The data are color-coded according to elevation angles. The times are in UTC.

706

707
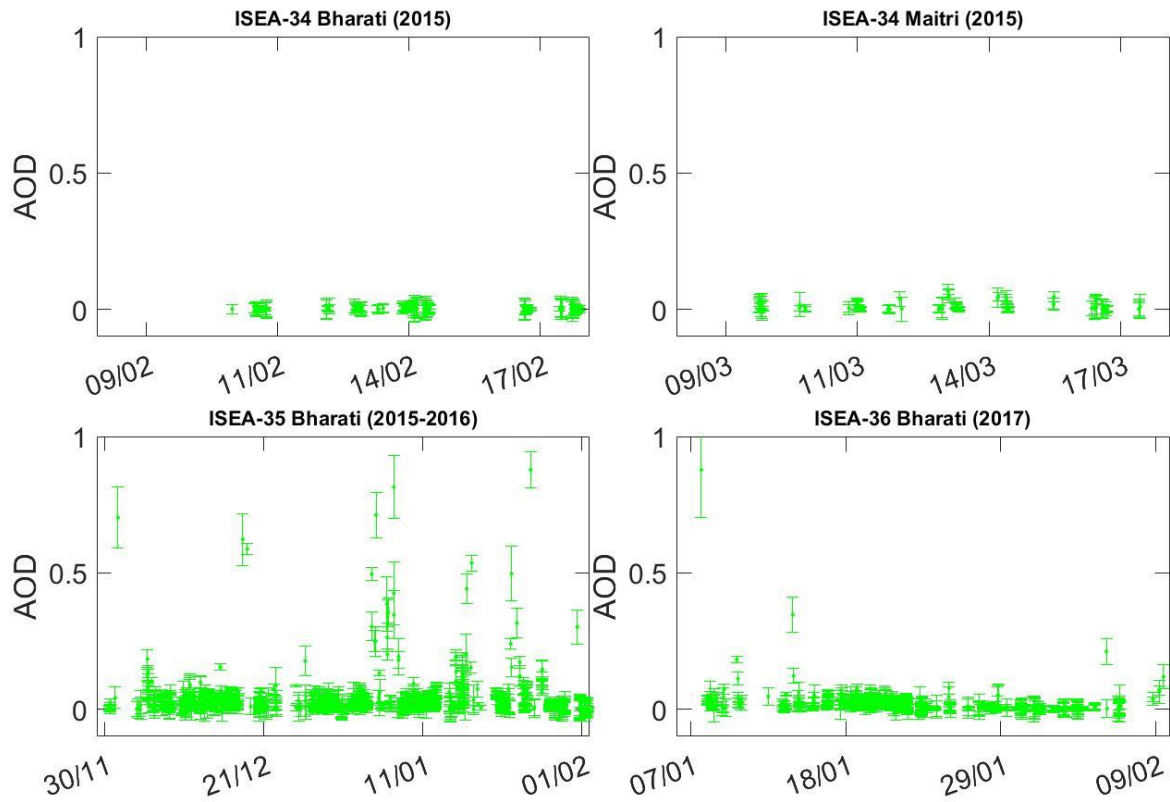
Figure 6: AOD timeseries retrieved using the O_4 DSCDs for all the four campaigns are shown. The data show only the 'good' datapoints, which are reliable and were mostly during clear sky conditions. The times are in UTC.
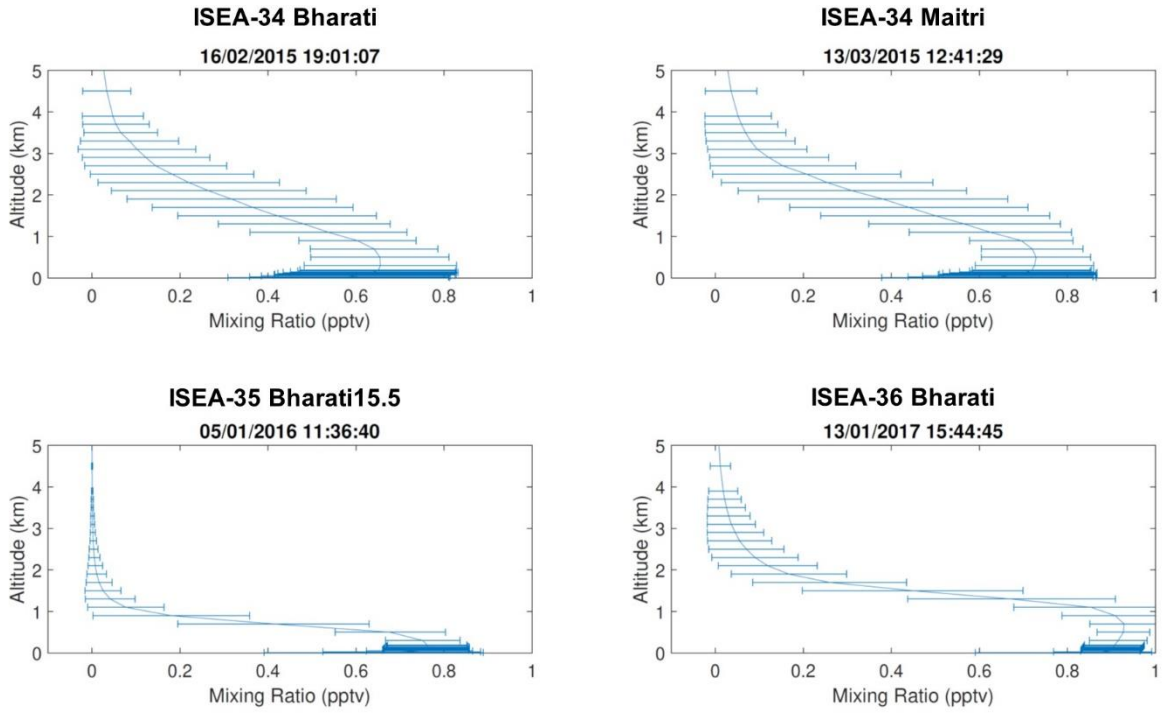
711

712
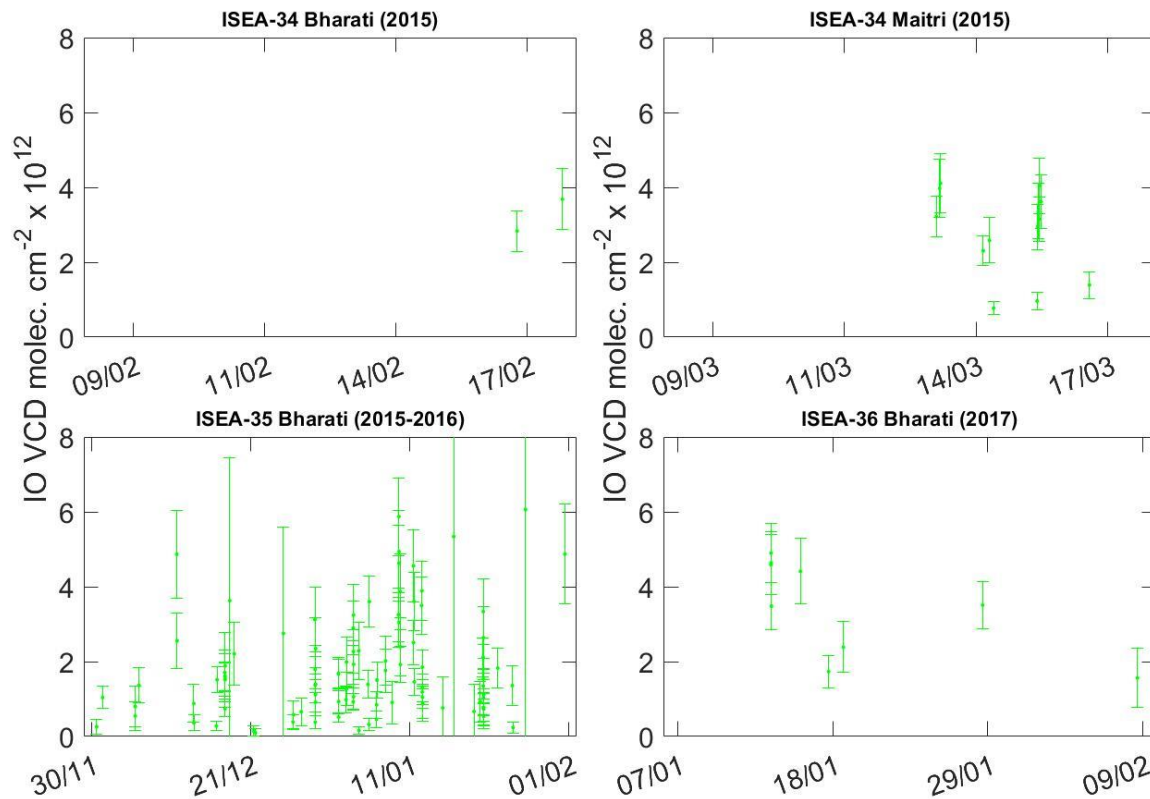
Figure 7: Observations of IO vertical column densities observed through all the four campaigns

are shown. These data were mostly during periods of clear sky, and where IO was observed above

the detection limit for most of the set elevation angles, enabling a reliable profile retrieval. The

times are in UTC.

717

39

718

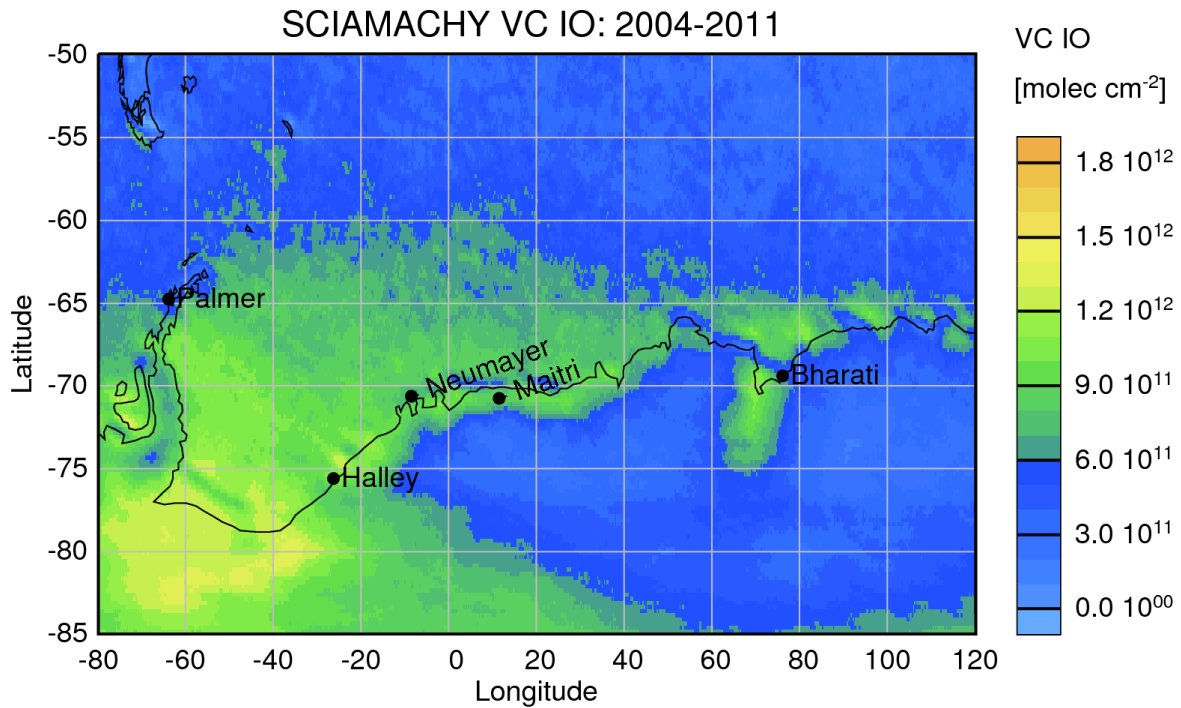**Figure 8:** Typical examples of IO vertical profiles retrieved during all the four campaigns are
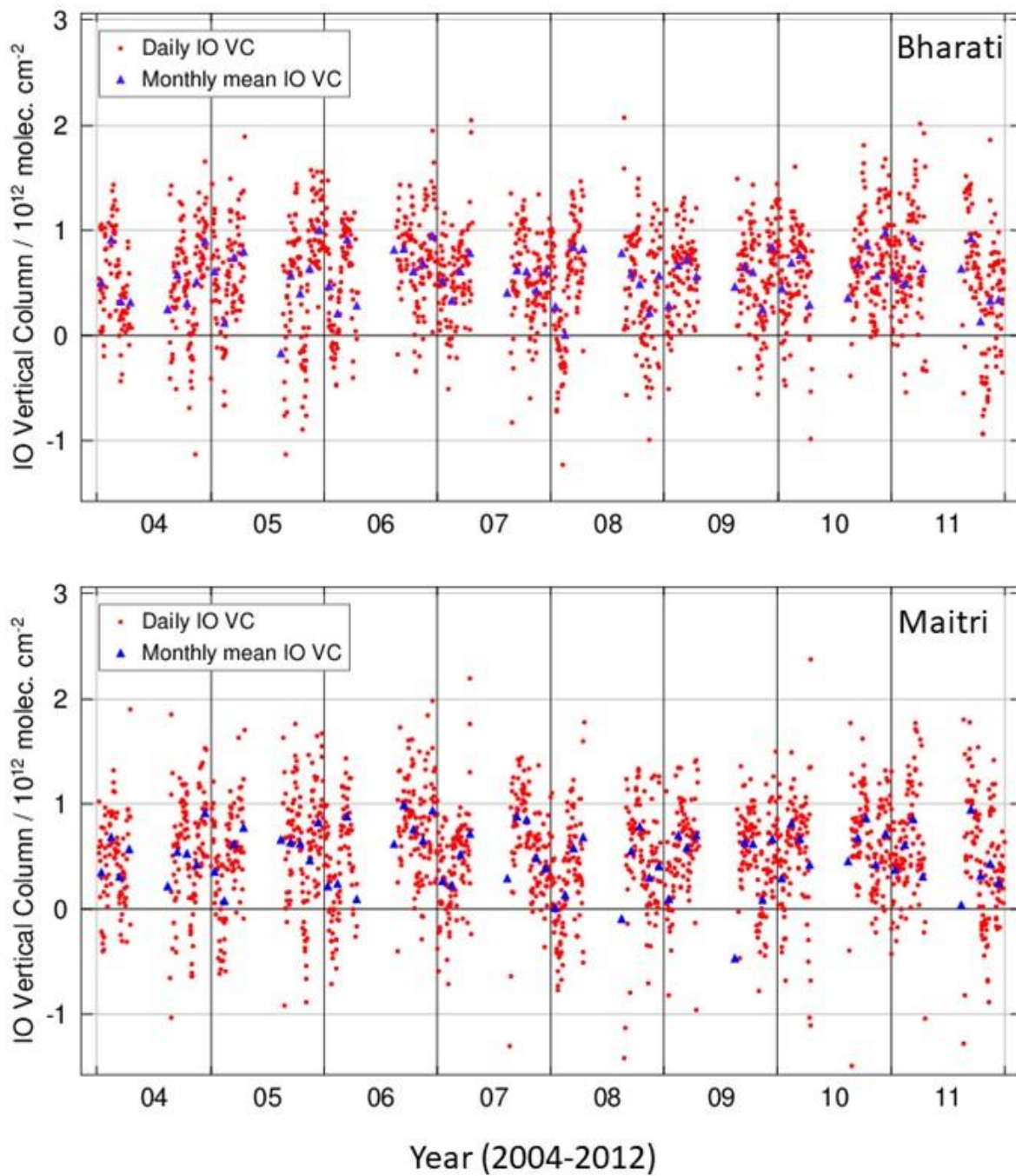
shown.

721

SCIAMACHY VC IO: 2004-2011

722

Figure 9: Averaged VCDs of IO as retrieved by SCIAMACHY between 2004-2011are shown.

Observations suggest that lower levels of IO are expected at Bharati and Maitri, as compared to

Halley Bay and Neumayer.

726

727

Figure 10: Timeseries of IO VCD observations at the Bharati station as retrieved by SCIAMACHY. The monthly mean values are shown in blue, and the daily datapoints are shown in red.